EREM 80/2
Journal of Environmental Research, Engineering and Management
Vol. 80 / No. 2 / 2024
pp. 118–132
10.5755/j01.erem.80.2.34693

Exploring the Influence of Various Land Use Land Cover on Land Surface Temperature of Coastal Tourism Areas in Bali Using Landsat 9

Received 2023/07 | Accepted after revisions 2024/04

https://doi.org/10.5755/j01.erem.80.2.34693

Exploring the Influence of Various Land Use Land Cover on Land Surface Temperature of Coastal Tourism Areas in Bali Using Landsat 9

I Wayan Diara[1], Ketut Dharma Susila[2], Wiyanti[2], I Nyoman Sunarta[3], Tati Budi Kusmiyarti[4], Moh Saifulloh[4,5]*

[1] Department of Environmental Science, Udayana University, Indonesia

[2] Faculty of Agriculture, Udayana University, Indonesia

[3] Faculty of Tourism, Udayana University, Indonesia

[4] Spatial Data Infrastructure Development Center, Udayana University, Indonesia

[5] Faculty of Marine Science and Fisheries, Udayana University, Indonesia

***Corresponding author:** m.saifulloh@unud.ac.id

The Bali Tourism area represents complex environments where human activities intersect with natural landscapes, resulting in diverse land use land cover (LULC) patterns. However, understanding the dynamics of LULC in these areas and its interaction with land surface temperature (LST) remains a challenge. This study addresses this gap by investigating LULC mapping in urban tourist destinations and its influence on LST variations. The research problem focuses on exploring the relationship between various land cover types and LST variations. The main objective is to assess the interaction of LULC variations with LST in urban tourist environments. To achieve this goal, an integrated approach combining remote sensing techniques and machine learning will be employed. LULC mapping will utilize support vector machine (SVM) techniques with datasets sourced from multi-channel data, and spectral indices such as enhanced built-up and bareness index (EBBI) and normalized differences vegetation index (NDVI) derived from Landsat 9. The findings present a vivid overview of the research area, where built-up areas dominate, and spanning 108.61 km^2. Other land cover classifications include rice fields/grasslands, plantation/perennial plants, barren land, mangrove forests, shrublands, and water bodies, accurately mapped with high precision (overall accuracy = 88.52% and Kappa = 81%). Maximum LST values peak in built-up and barren areas, reaching 29.89°C and 29.28°C, respectively, while other land cover types exhibit comparatively lower values. Our analysis of the spectral index used in LULC classification uncovers a positive correlation with EBBI (R^2 = 37.78%) and a negative

correlation with NDVI (R^2 = 10.69%, based on a substantial sample size of 67 869 pixels. We strongly urge future researchers to leverage high-resolution data for localized urban studies and stress the critical importance of enforcing stringent spatial planning regulations to safeguard green spaces, thus ensuring ecological equilibrium for future generations.

Keywords: land use land cover (LULC), land surface temperature (LST), remote sensing, environmental, urban tourism.

Introduction

Remote sensing plays a significant role in earth observation, environmental monitoring, agriculture, disaster management, and other fields (Bauer, 2020; García-Berná et al., 2020; Kaku, 2019). A prominent focus in remote sensing at the close of the 21st century is monitoring carbon stock/sequestration and climate change (Xiao et al., 2019; Yang et al., 2013). Anomalies characterize climate change through abrupt fluctuations in the Earth's surface temperature over short periods. Climate change affects temperature increases, such as changes in rain and snow patterns that fall to the surface, weather and seasons, and rising sea levels (Bellard et al., 2012). These changes can occur directly or indirectly as a result of human activities. Surface temperature changes can be assessed through in situ measurements or by estimation using remote sensing techniques. On a technical scale, remote sensing techniques provide time efficiency and the results close to in situ measurements with the right algorithm. Numerous thermal infrared (TIR) sensors are available with varying resolutions, including NOAA AVHRR, MODIS, ASTER, and, sensors from the Landsat TM/ETM+/OLI series (Kalma et al., 2008; Kuenzer et al., 2015; Weng, 2009). In our study, we use Landsat 9 satellite data for computing land surface temperature (LST) and detecting land use land cover in 2022. However, as of the end of the 21st century, no researchers have utilized remote sensing data derived from the Landsat 9 satellite. Landsat 9, an Earth observation satellite launched into space on September 27, 2021, from Launch Complex-3E, is equipped with Operational Land Imager 2 (OLI-2) and Thermal Infrared Sensor 2 (TIRS-2). OLI-2 captures Earth's surface observations in the near-infrared and short-wave bands, while TIRS-2 measures the thermal infrared radiation, or heat, emitted from the Earth and its surface.

Using remote sensing techniques efficiently measures the LST. Obtaining surface temperatures using satellite imagery is essential for analyzing global warming and climate change (Maimaitiyiming et al., 2014). Estimating the LST of objects on Earth becomes essential to assess the contribution of each object to the surface temperature. This is because each object or land cover has a different temperature. The change into an object with a high thermal capacity will cause the temperature to increase, as seen in urban or mining areas. Conversely, areas covered by forests or vegetation will experience temperature decreases. There is a relationship between green open areas and surface temperature in an area. The development of the area into built-up land contributes to increasing LST in urban areas and triggering climate change (Arshad et al., 2022; Dewan et al., 2021; Siddique et al., 2020). Built-up land includes not only a residential area but also roads connecting regions, which can lead to temperature increases. The increase in LST due to the development of urban areas has reached 2.26°C (Nurwanda and Honjo, 2020) to 8°C (Nurwanda and Honjo, 2020). The extent of temperature increase depends on location, season, and the area of land developed in urban settings.

This research case study was conducted in tourism and urban areas, specifically Denpasar and Kuta. Denpasar serves as the capital city center of Bali Province, while Kuta is renowned as a central hub for tourism. Previous researchers have highlighted Denpasar city's susceptibility to flooding and soil infiltration disturbances due to the prevalence of built-up land (Trigunasih and Saifulloh, 2022). Another issue plaguing this urban area is the consistent expansion of built-up land, resulting in air quality pollution (Sunarta and Saifulloh, 2022b, 2022a) and an annual increase in LST of 1°C between 2000 and 2020, as observed from Terra MODIS images (Sunarta et al., 2022). The development process must address the growing urban population and influx of tourists. Land use conversion from vegetated to non-vegetated areas can significantly impact site surface temperatures and, directly or indirectly, contribute to global warming phenomena.

Updating LULC mapping with the latest data derived from Landsat 9 is crucial for completing thematic map databases, particularly for local governments managing tourism areas. A significant challenge in LULC mapping is time-consuming drawing of boundaries, which requires a lot of workers to complete large areas (Nugraha et al., 2022). To address this challenge, we employ digital classification with a machine learning approach (Talukdar et al., 2020; Wang et al., 2022), specifically the SVM algorithm, which has demonstrated high accuracy across various satellite sensors, including Landsat TM, ETM+, OLI, and freely available imagery such as Sentinel 1/2, achieving accuracy rates exceeding 80% (Ghayour et al., 2021; Feizizadeh et al., 2023; Dagne et al., 2023). Incorporating LST interaction provides additional insights into how different objects on the Earth's surface respond to urban thermal conditions. These insights can guide the implementation of greening initiatives in specific tourism areas, thereby enhancing the comfort of tourists visiting Bali.

Methods

Study area

The research was conducted in the urban area of Denpasar and the tourism area of Kuta. Denpasar city is divided into four sub-districts (i.e., North Denpasar, East Denpasar, West Denpasar, and South Denpasar). The Kuta tourism area is administratively included in Badung Regency. For this study, only Kuta and North Kuta districts were selected. Both areas have experienced rapid tourism development, as evidenced by the increasing number of tourists and the expansion of built-up land. Geographically, the research case study is located at 115°10'00" E – 115°13'00" E and 08°36'00" S – 08°45'00" S. Based on biophysical conditions, the research area has an altitude of 0–50 meters above sea level, with a predominantly flat slope (0–8%). This area is located on the southern coast of Bali Province (*Fig. 1*).

Fig. 1. *Research site in Denpasar and Kuta, Bali Province*

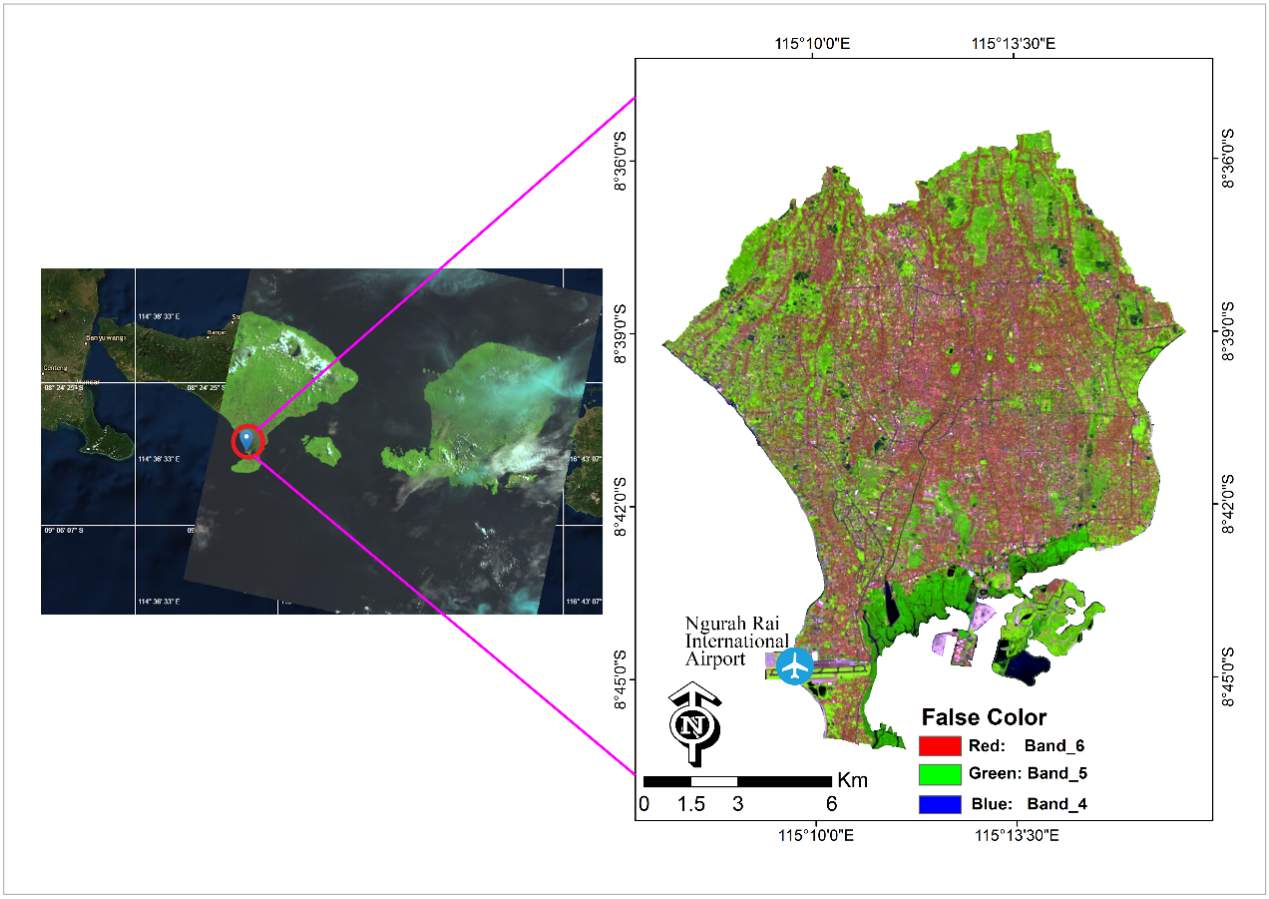

Bali's allure as a coastal tourism destination is undeniable, drawing a steady stream of international visitors year after year. However, beneath its picturesque landscapes lies a complex interplay between land use land cover (LULC) and the consequential land surface temperature (LST). Understanding these intricate relationships is paramount for sustainable development and effective urban planning in the region.

The count of foreign visitors identified at Ngurah Rai Airport and the surrounding Harbor exhibited an annual increment of 0.95% from 2010 to 2019 (Central Bureau of Statistics, 2023). This steady growth reflected the flourishing tourism sector of Bali, positioning it prominently on the global stage. However, the advent of the Covid-19 pandemic precipitated a significant downturn, impacting global destinations, including Bali's vibrant tourism sector (Sunarta and Saifulloh, 2022), with a pronounced dip of 11.98% in 2020 (*Fig. 2*). This staggering statistical shift underscores the critical need for comprehensive analysis, particularly regarding the LULC map and its associated LST dynamics.

Concurrently, recent investigations within the same domain have delved into the expanding footprint of built-up areas. These studies reveal a noteworthy expansion in built-up land from 2013 to 2021, witnessing an increase of 2.62 km^2, altering the landscape from 177.79 km^2 to 120.41 km^2 (Adnyana et al., 2023). This evolving urbanization trend accentuates the imperative of understanding how land transformation impacts LULC mapping and subsequent LST variations.

Fig. 2. *The annual number of foreign visitors to the Bali tourism area, particularly those detected through Ngurah Rai Airport and Harbor*

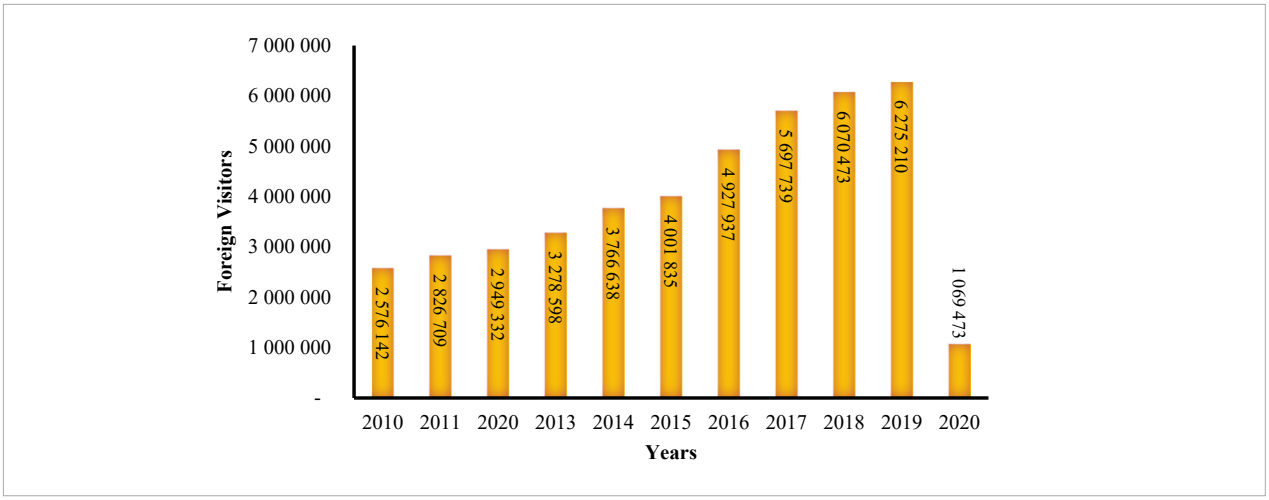

Tools and materials

Field data collection for training, testing, and validating our LULC map involved conducting field surveys using a Garmin Montana 680 GPS device, alongside manual digitization in the Google Earth Pro application. Satellite image processing was performed using the open-source QGIS 3.28.4 LTR application with the SCP Plugin library, and its machine learning classification utilized the Detzaka library. The primary data source for this study is the spectral bands from the Landsat 9 satellite. Remote sensing data collection was obtained from the USGS Earth Explorer Website (USGS, 2023). We selected a Landsat 9 image with minimal cloud cover to reduce image processing noise. The Landsat 9 data with the ID LC09_L1TP_116066_20220325_20220325_02_T1 was acquired on May 25, 2022. This image was captured in the Path 116 and Row 066 regions. Overall, the image scene used has less than 10% cloud cover, specifically in the tourism area at the time of the recording date, ensuring minimal bias during satellite imagery processing.

The instruments on Landsat 9 are enhanced replicas of Landsat 8, which already provides Earth observation data. The satellite carries two science instruments, the Operational Land Imager 2 (OLI-2) and the Thermal Infrared Sensor 2 (TIRS-2). OLI-2 captures observations of the Earth's surface in the near-infrared, near-infrared, and short-wave bands, and TIRS-2 measures the thermal infrared radiation, or heat, emitted from the Earth's surface. Landsat 9 improvements include a higher radiometric resolution for OLI-2

(14-bit quantization increased from 12-bit for Landsat 8) which allows the sensor to detect more delicate differences, especially in darker areas such as bodies of water and densely vegetated forests. In addition to the improved OLI-2, TIRS-2 has significantly reduced light stray compared with the Landsat 8 Thermal Infrared Sensor (TIRS), allowing for better atmospheric correction and more accurate LST measurements. Specifications of Landsat 9 data can be seen in *Table 1*.

Table 1. *Specification of Landsat 9 instrument*

Bands	Wavelength (μm)	Resolution (meters)
Band 1 – Coastal aerosol	0.43–0.45	30
Band 2 – Blue	0.45–0.51	30
Band 3 – Green	0.53–0.59	30
Band 4 – Red	0.64–0.67	30
Band 5 – Near Infrared (NIR)	0.85–0.88	30
Band 6 – SWIR 1	1.57–1.65	30
Band 7 – SWIR 2	2.11–2.29	30
Band 8 – Panchromatic	0.50–0.68	15
Band 9 – Cirrus	1.36 –1.38	30
Band 10 – Thermal infrared (TIRS) 1	10.60–11.19	100
Band 11 – Thermal infrared (TIRS) 2	11.50–12.52	100

Source: USGS, 2023

Data Analysis

Land use land over mapping

The mapping of LULC involves integrating remote sensing and machine learning. The images utilized for machine learning training and testing contain single-band spectral dataset (B2, B3, B4, B5, B6, and B7). To enhance the training image, we included spectral indices, namely NDVI and the enhanced built-up and bareness index (EBBI). EBBI can sensitively detect the difference between built and bare land, which has been found by As-syakur et al. (2012). The researcher quantified EBBI using NIR, SWIR, and TIRS channels (*Eq. 1*). The incorporation of a spectral index to the image aims to obtain the best LULC detection results, especially in urban areas dominated by built-up land. In this study, we classify LULC into seven types (i.e., built-up land, bare land, rice fields/grass, plantation/perennial plant, mangrove forest, shrubs, and water body). LULC variation data were sourced from the Geospatial Information Agency (BIG) in 2018, which will be updated with Google Earth imagery in 2022. The machine learning algorithm used is a support vector machine (SVM).

Training data were prepared and validated through the QGIS 3.28.4 LTR application. The training data consisted of 400 polygons, with a proportion of 70% for training and 30% for testing to run the SVM algorithm. The accuracy test utilized validation data comprising 320 points, strategically distributed. To maintain the independence of the model, we refrained from splitting the training/testing data for the validation process. Instead, the validation sample for the model was carried out on different data by referring to the high-resolution image of Google Earth in 2022.

$$EBBI = \frac{SWIR - NIR}{10\sqrt{SWIR - TIR}} \quad (1)$$

The support vector machine (SVM) is a supervised learning method commonly utilized for LULC classification. In classification modeling, SVM offers a more mature and clearer mathematical concept compared with other classification techniques. It is capable of addressing both classification and regression problems, whether linear or non-linear. For the classification task in this study, which involves seven land cover classes, SVM is particularly suitable (Mountrakis et al., 2011). In non-binary classification scenarios, such as multi-class classification, a kernel is essential for SVM to function effectively. The kernel facilitates the transformation of data into higher-dimensional space, enabling the SVM algorithm to delineate decision boundaries between different classes. Among various kernels, the radial basis function (RBF) kernel is widely regarded as the most effective for classification tasks (Osuna et al., 1997). Mathematically, the SVM algorithm is represented by *Eq. 2*, which outlines the process of determining the hyperplane based on support vectors, i.e., data points closest to other classes, and the kernel function, which defines the transformation of input data.

$$\text{RBF Kernels} : K(\ddot{x}i, \ddot{x}j) = \text{Exp}(-g\|xii\ 2), > 0 \quad (2)$$

The accuracy test was conducted using the SCP Plugin in the QGIS 3.28.4 LTR application. The output accuracy metrics include standard error (SE), producer accuracy (PA), user accuracy (UA), overall accuracy (OA), and Kappa. These metrics provide valuable insights into the performance of the classification model, assessing both its ability to correctly classify land cover types (PA and UA) and its overall effectiveness in accurately mapping the landscape (OA and Kappa).

Quantifications of land surface temperature (LST)

Quantification of LST was based on the formula and stages described in the sub-chapter. The theoretical understanding of each indicator in the LST calculation has been conveyed by Dash et al. (Dash et al., 2002). Spectral radiance correction is a correction that converts pixel value to spectral radiance value or top of atmosphere radiance value (*Eq. 3*). Our LST calculation utilizes both Band 10 (10.60–11.19 μm) and Band 11 (11.50–12.52 μm), which are then averaged to obtain the LST used to examine the relationship between each type of LULC in the research area. Combining the two thermal channels allows for enhanced accuracy and reliability in capturing surface temperature variations and mitigates the influence of atmospheric effects, thereby improving the overall quality of the LST data.

$$L_{\lambda} = (M_L \times Qcal) + A_L \quad (3)$$

Where: L_λ – spectral radiance on Landsat sensor (W/m^2-sr.μm); Q_{cal} – pixel value (DN); A_L – rescaling constant (radiance additive scaling factor for band (obtained from metadata file for band 10 and 11); M_L – radiance multiplicative scaling factor.

Spectral Reflectance Conversion (TOA Reflectance). Spectral reflectance conversion is a step to convert radiance value to actual reflectance value or real reflection value of an object on the Earth's surface. These values are used to extract object characteristics to analyze various information related to objects on the Earth's surface. Spectral reflectance conversion equation is published by USGS (2019) and uses pixel rescaling value which is provided in a metadata file (*Eq. 4*).

$$\rho_{\lambda'} = (M_\rho \times Q_{cal}) + A_\rho \quad (4)$$

Where: $\rho_{\lambda'}$ – spectral reflectance on Landsat sensor; Q_{cal} – pixel value (DN); M_ρ – multiplicative scaling factor for radiance; A_ρ – additive scaling factor for radiance.

The spectral radian value that has been obtained is then converted into a top-of-atmosphere brightness temperature, which is the effective temperature on the satellite, assuming a constant emissivity level. The equation used can be seen in *Eq. 5,* by using the thermal constants provided in the metadata file.

$$Tb = \frac{\mathrm{K2}}{Ln\left(\frac{K1}{L\lambda}+1\right)} - 273.15 \quad (5)$$

Where: Tb – TOA Brightness temperature (Kelvin); L_λ – TOA spectral radiance (watts / (m^2 x srad x μm)); K_1 – Band specific thermal conversion constant; K_2 – Band specific thermal conversion constant.

The normalized difference vegetation index (NDVI) is a widely utilized vegetation index for calculating surface temperature. It serves as an alternative method for estimating land surface emissivity. NDVI utilizes measurements from red and infrared wavelengths (bands 4 and 5), as depicted in *Eq. 6*.

$$NDVI = \frac{\mathrm{NIR+Red}}{\mathrm{NIR-Red}} \quad (6)$$

Proportion of vegetation / fractional vegetation cover (Pv) is fractional vegetation cover and the value is on a 0.00 to 1.00 scale (Sobrino and Raissouni, 2000). Pv requires scaled NDVI to reduce noise on LST caused by soil moisture and surface flux energy. Calculation of Pv is shown in *Eq. 7*.

$$Pv = \left(\frac{\mathrm{NDVI+NDVI}min}{\mathrm{NDVI}max-\mathrm{NDVI}min}\right)^2 \quad (7)$$

Land surface emissivity is energy emitted from an object. Landsat thermal sensors sense and record this energy so that the temperature of the object could be acquired. Calculation of emissivity is shown in *Eq. 8*.

$$\varepsilon = 0.004 \times \mathrm{P}v + 0.986 \quad (8)$$

The last step is LST quantification based on the data derivatives that have been calculated in the previous process. The calculation of the LST value can be seen in *Eq. 1.9*.

$$LST = \frac{Tb}{\left\{1+\left[\left(\frac{\lambda Tb}{c2}\right)Ln\ \varepsilon\lambda\right]\right\}} \quad (9)$$

Where: Tb – Temperature brightness (°C); λ – Central wavelength of emitted radiance; ε – Emissivity; *Ln* – mathematical function for the natural logarithm.
$c2 = h * \frac{c}{s} = 1.4388 * 10^{-2}\mathrm{mK} = 14388\ \mu\mathrm{m\ K}.$

Results and Discussion

Mapping of land use land cover

This sub-chapter presents the results of the LULC classification in tourism areas. Before delving into the results, we show the spectral indices of the enhanced built-up and bareness index (EBBI) and the normalized difference vegetation index (NDVI). Both spectral indices are utilized as input stacking images with other single bands. The minimum, maximum, and mean values, and the standard deviations are as follows: –0.72, 0.93, 0.51, and 0.19 (*Table 2*). NDVI represents the greenness level and tan vegetation, so the higher value represents the condition of dense vegetation cover on the Earth's surface (Weng et al., 2004). The dark blue zone is high-density vegetation that is dominantly found in the northern and southern regions (*Fig. 3a*). For EBBI, the minimum, maximum, mean, and standard deviation values are –0.11, 0.79, 0.07, and 0.06, respectively (*Table 2*). EBBI is inversely related to NDVI, as higher spectral index values indicate areas with high building density, including bare land. The spatial distribution of EBBI reveals that high values dominate the case study area, as indicated by the orange and red zones (*Fig. 3b*).

Table 2. *Statistical value of spectral index*

Parameters	Min	Max	Mean	SD
NDVI	–0.72	0.93	0.51	0.19
EBBI	–0.11	0.79	0.07	0.06

In our scientific article, the LULC types encompass built-up areas, bare land, rice fields/grass, plantation/perennial plants, mangrove forests, shrubs, and water bodies. Built-up land use comprises housing, shops, offices, hotels, supermarkets, road networks, parking lots, and airports. Bare land areas include stretches of beach sand, landfill areas, and other vegetation-free zones. Rice fields are characterized by rice cultivation, alongside crops like corn, vegetables, and other agricultural commodities, including grasslands. Plantations/perennial plants feature dense canopy cover and annually replenished plants with distinct woody characteristics. This category encompasses green open spaces, roadside trees, and shade trees within hotel premises.

In our research case study, mangrove forests are spatially clustered, facilitating easy identification. They are closely associated with water bodies, predominantly situated in the southern coastal region. Shrubs

Fig. 3. *Spatial distribution of EBBI (a) and NDVI (b)*

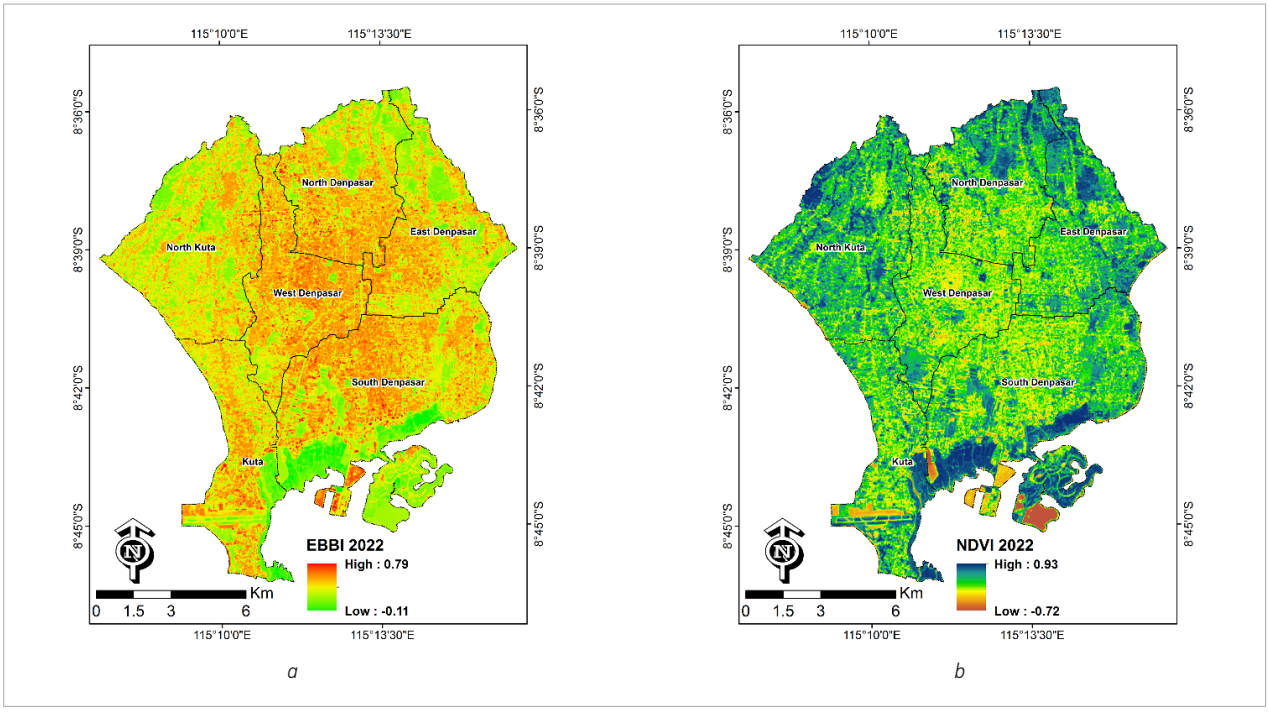

represent areas with sparse annual vegetation density. Water bodies encompass marine areas, ponds, and other water bodies. The spectral signature depicted in *Fig. 4* illustrates the interplay between wavelength and spectral values following atmospheric correction using the dark object subtraction method, specifically targeting channels B2 (Blue), B3 (Green), B4 (Red), B5 (NIR), B6 (SWIR 1), and B7 (SWIR 2). Additionally, EBBI and NDVI were incorporated into the stacked image.

In the R-G-B channels, built-up and bare land objects exhibited the highest spectral values. Conversely, vegetated objects displayed elevated spectral values in the NIR channel, indicating a strong correlation with NDVI. Water bodies and built-up land showed minimal spectral responses in the NIR channel and vegetation index. SWIR-1 and SWIR-2 channels, alongside EBBI, demonstrated sensitivity to built-up land objects, characterized by their heightened spectral values (*Fig. 4*). Conversely, they displayed lower sensitivity to vegetated objects, as evidenced by their diminished spectral values. This analysis highlights the distinct spectral characteristics of different land cover types in the study area. The correlation between spectral signatures, land cover indices, and various remote sensing channels offers valuable insights for land cover classification and monitoring, particularly in urban and vegetated environments.

Fig. 4. *The spectral signatures in various objects*

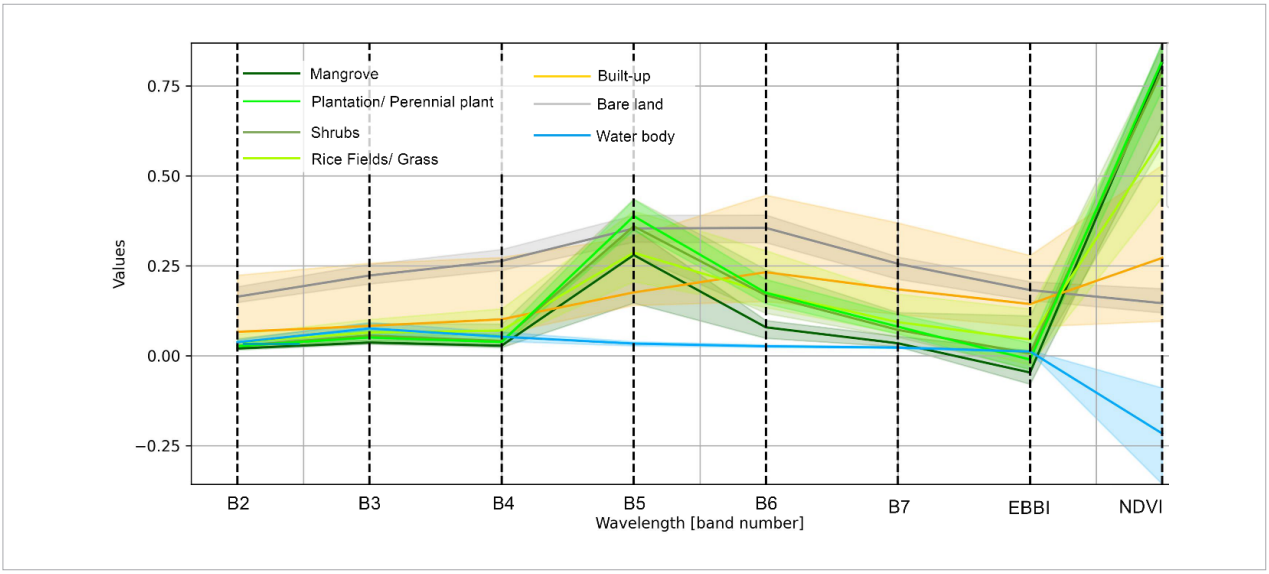

The average standard error (SE) value for each LULC is 0.01. Based on the producer accuracy (PA) value, the plantation/perennial plant type LULC has the lowest value of 56.98%, and others have a value of > 80%. User accuracy (UA) < 80% was found in bare land (50%), shrubs (55.56%), and perennial plants (72.73%). The highest Kappa hat values were found in water bodies (1.00), mangrove forests (1.00), and built-up land (0.91), while other LULC < 0.8. Several factors contribute to the low accuracy of this land cover classification. One significant factor is the spectral bias between cover types, leading to misclassification. For instance, bare land areas exhibit spectral variations similar to built-up land, while large expanses of rice fields may contain unplanted areas (bare land) at varying elevations, further complicating the classification process and reducing accuracy. Additionally, in shrubland areas, the spectral values of all parameters used in the LULC model tend to exhibit similar patterns and values. Furthermore, the differentiation of vegetation types within the study area adds complexity, contributing to decreased accuracy.

The overall accuracy of the LULC model with the SVM algorithm is 88.52%, with a Kappa value of 81% (*Table 3*). The producer's accuracy value serves as a thematic assessment, which shows the level of truth of the classification results against conditions in the field. We replace the field data with reference to the Google Earth Imagery in 2022. User accuracy describes the accuracy of the classification results for all identifiable objects.

Total accuracy represents the value of the total accuracy of the appearance of objects that are correct on the classification map with the field. The Kappa index value considers the classification process error factor, so the Kappa index value is lower than the total accuracy value, which only finds the correct data between the classification results and field conditions. Total accuracy describes the value of the total accuracy of the appearance of objects that are correct on the classification map with the field. An 81% Kappa value indicates that the digitally mapped LULC using SVM is classified as very high. Kranjčić et al. (2019) state that the range of Kappa values is very high, with values exceeding 80%, falling into the high category, followed by 61–80% in the moderate category, and 41–60% in the low category.

The results of the LULC classification reveal that built-up areas dominate, covering an expanse of 108.61 km^2. Following closely are rice fields/grass, sprawling over 42.37 km^2, followed by plantation/perennial plants (11.95 km^2), bare land (10.04 km^2), mangrove forests (6.84 km^2), shrubs (4.78 km^2), and water bodies (2.69 km^2), as depicted in *Fig. 5*. The spatial distribution of built-up land is delineated by the orange zone, predominantly saturating urban and tourism hubs (*Fig. 6a*). Verdant stretches are characterized by green and dark green hues, indicating rice fields/grass, plantation/perennial plants, shrubs, and mangrove forests. Additionally, patches of bare land and water bodies dot the southern coastal region (*Fig. 6*).

Assessing the impact of various LULC on LST

In the lowest elevation research locations, the LST was found to be 19.27°C in water bodies and rice fields, with mangrove forests registered 19.42°C. The highest maximum LST values were observed in built-up areas and bare land, with 29.89°C and 29.28°C, respectively. Other LULC types, such as plantations/perennial plants, exhibited relatively high maximum values of 27.87°C and 27.14°C, followed by shrubs, mangrove forests, and water bodies, with LST values of 24.90°C, 24.60°C, and 23.97°C, respectively.

The highest mean LST value was found in built-up areas at 25.50°C, followed by other land cover types, including bare land, rice fields/grass, plantations/perennial plants, shrubs, mangroves, and water bodies, with

Table 3. *Accuracy assessment of LULC types based on SVM algorithm*

No	LULC types	SE	PA (%)	UA (%)	Kappa hat	OA (%)	Kappa (%)
1	Built-up land	0.01	94.36	96.22	0.91	88.52	81.00
2	Bare land	0.01	89.64	50.00	0.48		
3	Rice field/ grass	0.01	82.27	83.08	0.78		
4	Plantation/ perennial plant	0.01	56.98	72.73	0.71		
5	Mangrove forest	0.00	85.99	100	1.00		
6	Shrubs	0.00	100.00	55.56	0.55		
7	Water body	0.00	100.00	100	1.00		

Fig. 5. *Graph of difference LULC types and coverage area*

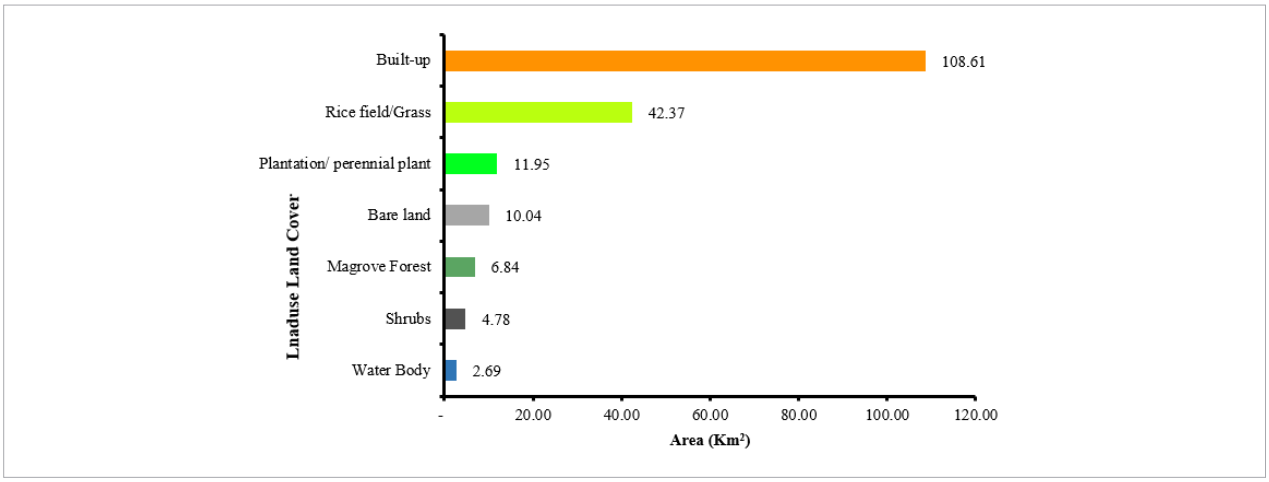

respective values of 25.50°C, 24.97°C, 24.62°C, 24.22°C, 22.71°C, 21.97°C, and 21.39°C (*Table 4*). Based on their standard deviation values, water bodies, bare land, rice fields/grass, and built-up areas exhibited relatively high variability, with values of 1.27, 1.13, 1.03, and 0.90, respectively.

These findings suggest that these four land cover types exhibit high variability in their interactions with LST. For example, in water body areas with varying water depths and sediment presence, diverse interactions with LST were observed. Similarly, built-up areas, bare land, and rice fields/grass displayed varying characteristics in specific regions, including differences in vegetation density and non-vegetated areas. For instance, in rice field areas, both bare land zones and waterlogged rice areas were identified, resulting in relatively varied responses to LST.

Table 4. *The differences LULC types on LST (°C)*

LULC	Min	Max	Mean	Std
Built-up land	20.82	29.89	25.50	0.90
Bare land	20.01	29.28	24.97	1.13
Rice field/grass	19.23	27.14	24.62	1.03
Shrubs	20.72	24.90	22.71	0.58
Plantation/perennial plant	21.89	27.87	24.22	0.78
Mangrove forest	19.42	24.60	21.97	0.78
Water body	19.23	23.97	21.39	1.27

The spatial distribution of built-up land, as observed in accordance with the most recent advancements in urban ecology and land cover analysis, prominently extends across urban regions and tourist destinations while intriguingly encompassing the eastern and southwestern coastal regions. In the southern coastal sector of urban zones, an intriguing interplay of land cover types characterized by notably high vegetation density, such as thriving mangrove forests and robust shrubbery, emerges. Spatially, the Kuta tourism area features an expanded runway and parking lot within the vicinity of Ngurah Rai International Airport, where bare land is delineated as a gray zone on the map. The surrounding region is predominantly characterized by built-up land in the form of an airplane runway, while the area within the airport premises comprises a grassland landscape.

Furthermore, the verdant tapestry of additional vegetative covers, including rice fields/grass and plantations, adorns the fringes of urban and tourist areas. This nuanced arrangement has been notably accentuated in light of recent research, as the central urban sectors have become increasingly synonymous with a prevailing dominance of built-up land (*Fig. 6*).

Fig. 6. *Spatial distribution of LULC types based on SVM machine learning algoritm (a) and LST in urban and tourism areas (b)*

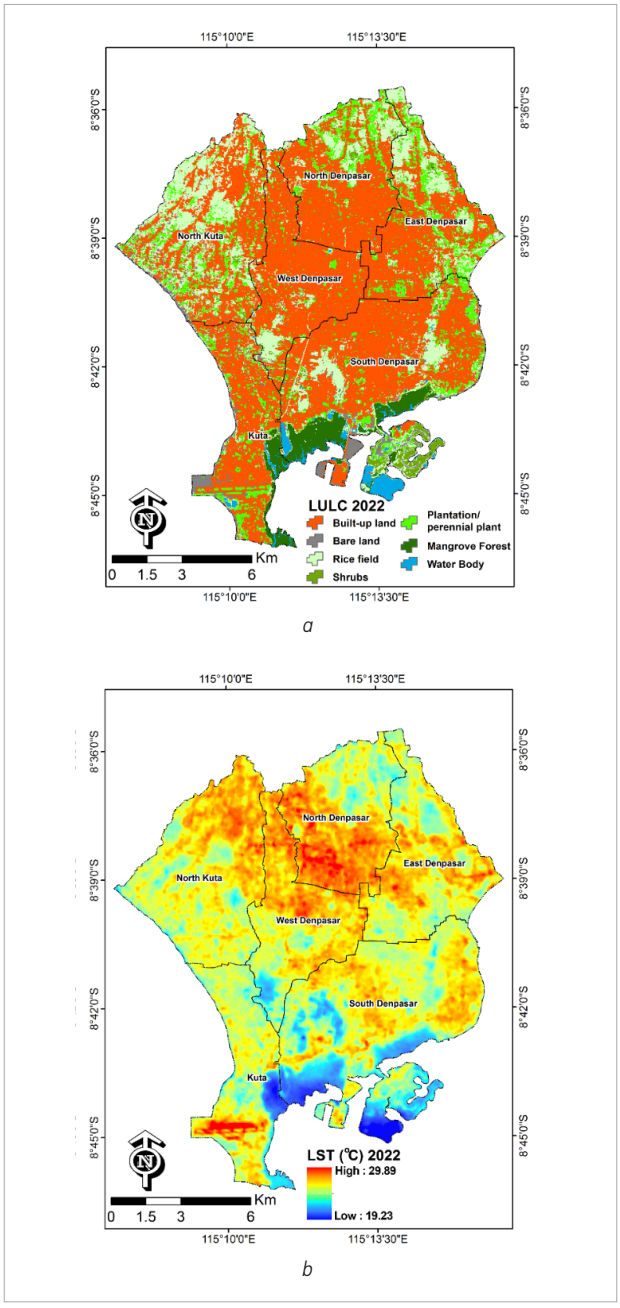

Remarkably, this spatial pattern intimately corresponds to contemporary investigations into LST dynamics. The most current research has unveiled the central urban core as a focal point of interest, depicted in vivid shades of red on LST maps, signifying heightened LST values and aligning with the well-established urban heat island effect (Wirayuda et al., 2023; Sunarta et al., 2022). A recent study found that in the Denpasar Tourism Area, the maximum LST value measured using Landsat 8 imagery acquired on September 9, 2022, was 26.2°C (Wirayuda et al., 2023). Overall, the spatial pattern we observed aligns with the findings of previous researchers, although the maximum LST values differ due to the previous researchers' focus solely on the Denpasar City area and the different acquisition and sensor types of satellite imagery. Conversely, the southern coastal regions have come into a sharper focus as the epicenter of lower LST values, prominently illuminated in deep shades of blue. Meanwhile, peripheral vegetated areas on the urban peripheries emerge in subtler shades of light blue, underscoring the complex interplay between land LULC and LST patterns within these evolving urban and coastal landscapes.

We present scatterplots based on raster data comprising a total of 67 869 pixels. These figures offer profound insights into the correlations between EBBI and LST, as well as between NDVI and LST. Initially, our analysis accentuates a positive correlation between EBBI and LST (R^2 = 37.78%). This positive relationship is vividly illustrated by the upward-sloping regression line. Conversely, upon scrutinizing the association between NDVI and LST, we discern a negative correlation (R^2 = 10.69%), delineated by a downward-sloping regression line (*Fig. 7*). The findings in our study hold particular significance for urban landscapes. The correlation between EBBI, NDVI, integrated into the LULC model, and their interaction with LST play a pivotal role in understanding land cover dynamics. As stated by As-syakur et al. (2012) and Hishe et al. (2024), EBBI, functioning as a spectral index, delineates built-up areas and unveils barren surfaces, providing insights into urbanization trends and land degradation. Elevated EBBI values signify dense built-up regions or barren expanses. Conversely, previous researchers (Chen and Zhang, 2017; Alexander, 2020) have noted that NDVI measures vegetation density and vitality, portraying healthier vegetation cover through higher values. The interplay among these indices and LST reveals how land cover types influence surface temperature dynamics. For instance, areas characterized by built-up structures and barren landscapes, which typically exhibit lower vegetation density, tend to manifest higher surface temperatures due to heightened heat absorption and diminished cooling from evapotranspiration. Conversely, regions showcasing dense vegetation cover, as indicated by higher NDVI values, often exhibit lower surface temperatures due to shading effects and increased transpiration rates.

Fig. 7. *Scatterplot depicting the relationship between the built-up land index (EBBI) and LST (a), and the relationship between the vegetation index (NDVI) and LST (b)*

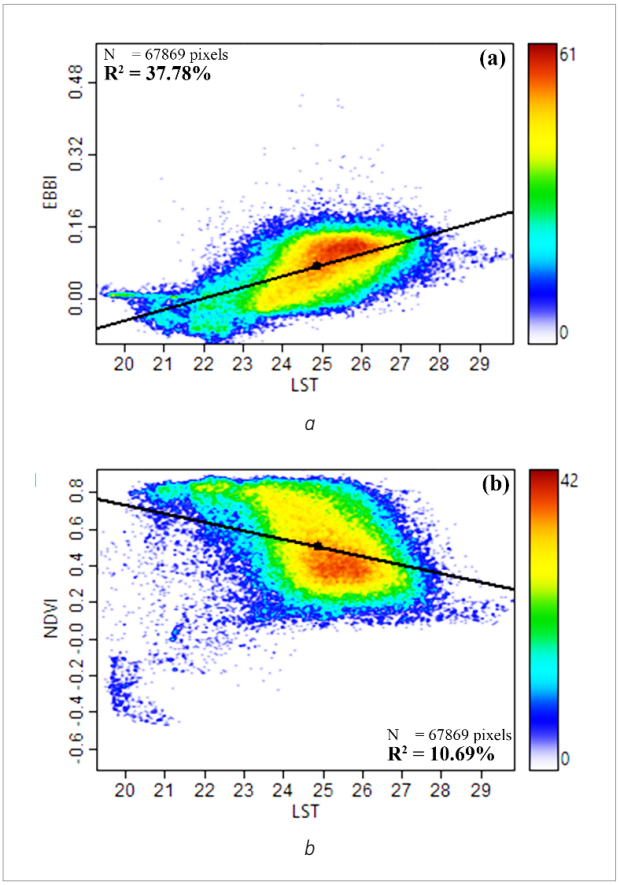

The LST map presented in *Fig. 5* is the result of averaging calculations using thermal channels 10 and 11 from Landsat 9. To understand the interaction between thermal channels and land cover, we compared the products from the Thermal Infrared Sensor 2 (TIRS-2) on Landsat 9 with TIRS-1 on Landsat 8. Landsat 8 data were acquired on March 17 and August 24, 2022, while Landsat 9 data were acquired on March 25 and

August 16, 2022, with an 8-day acquisition interval for both products. We selected one pixel for each land cover type and extracted the LST values from the products generated by both sensors using bands 10 and 11. Generally, LST values derived from thermal channel 10 were higher than those from channel 11, for both TIRS-1 and TIRS-2 sensors. Both sensors exhibited similar patterns in channels 10 and 11 after testing on various land cover types. Overall, the highest LST values were observed in built-up and bare land areas (*Fig. 8*).

Fig. 8. *The response of land cover variations on land surface temperature (LST) sourced from different sensors, namely TIRS-1 on Landsat 8 and TIRS-2 on Landsat 9, as well as from different thermal channels, channel 10 and channel 11*

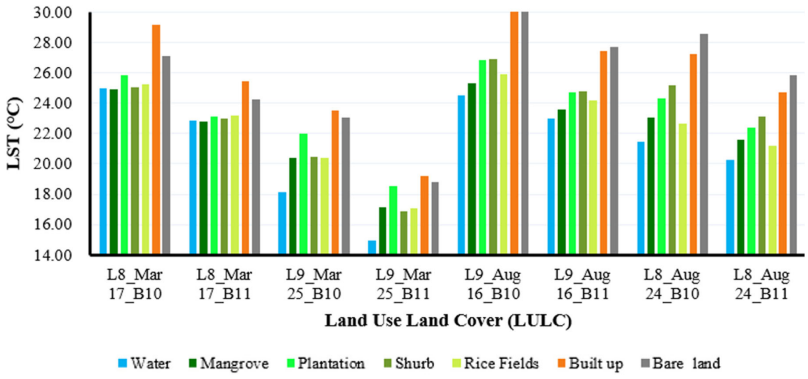

The launch of the TIRS-2 sensor on Landsat 9 offers significant advantages for future researchers, particularly in estimating LST with an 8-day temporal resolution. The varying LST values across different objects indicate diverse interactions, and the differences in data acquisition also highlight variations in LST influenced by regional climate variability. This technological advancement enhances our ability to monitor and analyze land surface temperature dynamics, providing valuable insights into the impacts of land cover changes and climate variability on urban and natural environments.

A study by As-syakur et al. (2012), utilizing Landsat 5 TM and 7 ETM+ data, revealed that, in 1995, LST ranged from 23.18°C to 31.04°C, averaging 27.28°C, while in 2003, ground surface temperatures varied from 21.78°C to 36.12°C, with an average of 29.44°C. Notably, the standard deviation (SD) and LST variance in 1995 were lower compared with 2003, indicating slightly higher LST variation in the latter year. These findings diverge significantly from our study, where LST values ranged from 19.23°C to 29.89°C based on Landsat 9 data acquired on May 25, 2022. Moreover, the Landsat 9 LST product exhibited a strong agreement with Landsat 7/8 LST, displaying a mean bias of 0.25/0.08 K, RMSE of 0.51/1.04 K, and mean absolute error of 0.38/0.64 K. This consistency in performance across Landsat 7/8/9 LST products can be attributed to the uniformity of the LST retrieval algorithm, although variations in specific heat capacity and thermal inertia among different land surface covers may contribute to significant biases (Meng et al., 2022).

The significant disparities in LST observed compared with previous studies can be attributed to the influence of global climate anomalies, particularly the El Niño and La Niña phenomena. According to the Oceanic Niño index (ONI), moderate El Niño events occurred in 1995 and 2003, while a moderate La Niña event was active from 2021 to 2022. El Niño is characterized by elevated sea surface temperatures in the central Pacific Ocean, promoting cloud formation and reducing rainfall in Indonesia, consequently leading to drought conditions and heightened temperatures. Conversely, La Niña entails cooler sea surface temperatures in the central Pacific, diminishing cloud formation, increasing rainfall, humidity, and correlating with decreased temperatures. These climate phenomena play a crucial role in shaping regional weather patterns and can significantly impact land surface temperatures.

Apart from the influence of global climate, a recent study (Hashim et al., 2022) conducted in Baghdad, Iraq, informed that the highest LST was associated with residential and arid areas, ranging from 46.7°C to 52.7°C, while the lowest

was with water bodies and gardens, ranging between 25°C and 30.4°C. Research in the Dhaka-Bangladesh metropolitan area predicts an increase in LST 2020 to 2030 in summer and winter to be greater than 35°C (Roy et al., 2020). Another researcher states that the increase in built-up land and urban expansion contributes to the rise in LST (Hua and Ping, 2018; Rahman et al., 2023; Ranagalage et al., 2017). Other effects are decreasing environmental quality, decreasing urban carbon stocks, and urban socio-economic problems (Chu et al., 2020; Lindén et al., 2020; Babalola and Akinsalola, 2016; Zhou et al., 2022). For future researchers, we recommend using remote sensing imagery with higher spatial and temporal resolution for LULC and LST investigations in small urban areas to address the research gaps or limitations in this study. This approach will yield more accurate results on LST variability patterns for each season and their impact on climate change and the local environment.

Conclusions

The integration of remote sensing and the SVM machine learning algorithm facilitates the analysis of Landsat 9 data, enhancing LULC mapping and precise LST computation. Our study reveals distinct LST values across different LULC categories, with built-up areas dominating at 108.61 km^2, followed by rice fields/grass (42.37 km^2), plantation/perennial plants (11.95 km^2), bare land (10.04 km^2), mangrove forests (6.84 km^2), shrubs (4.78 km^2), and water water bodies (2.69 km^2). The highest LST values were recorded within built-up and barren land regions, reaching 29.89°C and 29.28°C, respectively, while other land cover types exhibit comparatively lower values. Our LULC classification achieved an overall accuracy of 88.52% and a Kappa coefficient of 81%, indicating accurate mapping with high precision. Additionally, our analysis of the spectral index used in LULC classification uncovers a positive correlation with EBBI (R^2 = 37.78%) and a negative correlation with NDVI (R^2 = 10.69%), based on a substantial sample size of 67 869 pixels. These findings underscore the significant variability in LST interactions with primary land cover types, influenced by factors such as built-up areas, vegetation density, and water bodies. Future researchers should leverage high-spatial-resolution data with extended temporal coverage, especially for local/small urban-scale studies. Moreover, we recommend that local governments enforce regulations on spatial planning to preserve green open spaces, crucial for maintaining environmental equilibrium. Additionally, we propose that these findings serve as guidance in urban planning, advocating for regulations to limit the construction of tourism facilities in coastal tourism areas. Such restrictions are essential as they can mitigate the increase in surface temperatures, thereby addressing concerns related to the urban heat island phenomenon in the future.

Acknowledgements

This research received a grant from the Institute for Research and Community Service at Udayana University with contract number: B/1.48/UN14.4.A/PT.01.03/2023 and B/255.620/UN14.4.A/PT.01.03/2024

References

Andyana I., As-syakur A., Sunarta I., Suyarto R., Diara I., Susila K., Saifulloh M., Kusmiyarti T., Wiyanti W. (2023) Urban tourism expansion monitoring by remote sensing and random forest. IOP Conference Series: Earth and Environmental Science 1180(1): 012046. Available at: https://doi.org/10.1088/1755-1315/1180/1/012046

Alexander C. (2020) Normalised difference spectral indices and urban land cover as indicators of land surface temperature (LST). International Journal of Applied Earth Observation and Geoinformation 86: 102013. Available at: https://doi.org/10.1016/j.jag.2019.102013

Arshad S., Ahmad S. R., Abbas S., Asharf A., Siddiqui N. A., Islam Z. ul. (2022) Quantifying the contribution of diminishing green spaces and urban sprawl to urban heat island effect in a rapidly urbanizing metropolitan city of Pakistan. Land Use Policy 113. Available at: https://doi.org/10.1016/j.landusepol.2021.105874

As-syakur A.R., Adnyana I. W. S., Arthana I. W., and Nuarsa I. W. (2012) Enhanced built-UP and bareness index (EBBI) for mapping built-UP and bare land in an urban area. Remote Sensing 4(10). Available at: https://doi.org/10.3390/rs4102957

As-syakur A. R., Nuarsa I.W., Arthana I.W., Mahendra M.S., Adnyana I.W.S., Merit I. N., Suyarto R., Lila K.A. (2012) Remote Sensing Image-Based Analysis of the Urban Heat Island in Denpasar , Indonesia. 8th International Symposium on Lowland Technology.

Bauer M.E. (2020) Remote Sensing of Environment: History, Philosophy, Approach and Contributions, 1969 -2019. Remote Sens-

ing of Environment 237. Available at: https://doi.org/10.1016/j.rse.2019.111522

Bellard C., Bertelsmeier C., Leadley P., Thuiller W., and Courchamp F. (2012) Impacts of climate change on the future of biodiversity. In Ecology Letters 15(4). Available at: https://doi.org/10.1111/j.1461-0248.2011.01736.x

Central Bureau of Statistics Bali Province. Available at: https://bali.bps.go.id/indicator/16/106/1/number-of-monthly-foreign-visitor-to-bali-by-gate.html (accesssed 9 December 2023).

Chen X., and Zhang Y. (2017) Impacts of urban surface characteristics on spatiotemporal pattern of land surface temperature in Kunming of China. Sustainable Cities and Society 32: 87-99. Available at: https://doi.org/10.1016/j.scs.2017.03.013

Chu L., Oloo F., Chen B., Xie M., and Blaschke T. (2020) Assessing the influence of tourism-driven activities on environmental variables on hainan island, china. Remote Sensing 12(17). Available at: https://doi.org/10.3390/rs12172813

Dagne S. S., Hirpha H. H., Tekoye A. T., Dessie Y. B., and Endeshaw A. A. (2023). Fusion of sentinel-1 SAR and sentinel-2 MSI data for accurate Urban land use-land cover classification in Gondar City, Ethiopia. Environmental Systems Research 12(1): 40. Available at: https://doi.org/10.1186/s40068-023-00324-5

Dash P., Göttsche F. M., Olesen F. S., and Fischer H. (2002) Land surface temperature and emissivity estimation from passive sensor data: Theory and practice-current trends. International Journal of Remote Sensing 23(13). Available at: https://doi.org/10.1080/01431160110115041

Dewan A., Kiselev G., Botje D., Mahmud G. I., Bhuian M. H., and Hassan Q. K. (2021) Surface urban heat island intensity in five major cities of Bangladesh: Patterns, drivers and trends. Sustainable Cities and Society 71. Available at: https://doi.org/10.1016/j.scs.2021.102926

Feizizadeh B., Omarzadeh D., Kazemi Garajeh M., Lakes T., and Blaschke T. (2023). Machine learning data-driven approaches for land use/cover mapping and trend analysis using Google Earth Engine. Journal of Environmental Planning and Management 66(3): 665-697. Available at: https://doi.org/10.1080/09640568.2021.2001317

García-Berná J. A., Ouhbi S., Benmouna B., García-Mateos G., Fernández-Alemán J. L., and Molina-Martínez J. M. (2020) Systematic mapping study on remote sensing in agriculture. Applied Sciences (Switzerland) 10(10). Available at: https://doi.org/10.3390/app10103456

Ghayour L., Neshat A., Paryani S., Shahabi H., Shirzadi A., Chen W., and Ahmad A. (2021) Performance evaluation of sentinel-2 and Landsat 8 OLI data for land cover/use classification using a comparison between machine learning algorithms. Remote Sensing 13(7): 1349. Available at: https://doi.org/10.3390/rs13071349

Hashim B. M., Al Maliki A., Sultan M. A., Shahid S., and Yaseen Z. M. (2022) Effect of land use land cover changes on land surface temperature during 1984-2020: a case study of Baghdad city using landsat image. Natural Hazards 112(2). Available at: https://doi.org/10.1007/s11069-022-05224-y

Hishe S., Gidey E., Zenebe A., Girma A., Dikinya O., Sebego R., and Lyimo J. (2024) Urban heat island and ecological condition modeling using thermal remote sensing in Tigray-Northern Ethiopia. Modeling Earth Systems and Environment 10(1): 735-749. Available at: https://doi.org/10.1007/s40808-023-01804-4

Hua A. K., and Ping O. W. (2018) The influence of land-use/land-cover changes on land surface temperature: a case study of Kuala Lumpur metropolitan city. European Journal of Remote Sensing 51(1). Available at: https://doi.org/10.1080/22797254.2018.1542976

Kaku K. (2019) Satellite remote sensing for disaster management support: A holistic and staged approach based on case studies in Sentinel Asia. In International Journal of Disaster Risk Reduction 33. Available at: https://doi.org/10.1016/j.ijdrr.2018.09.015

Kalma J. D., McVicar T. R., and McCabe M. F. (2008) Estimating land surface evaporation: A review of methods using remotely sensed surface temperature data. Surveys in Geophysics 29(4-5). Available at: https://doi.org/10.1007/s10712-008-9037-z

Kranjčić N., Medak D., Župan R., and Rezo M. (2019) Support vector machine accuracy assessment for extracting green urban areas in towns. Remote Sensing 11(6): 655. https://doi.org/10.3390/rs11060655

Kuenzer, C., Dech, S., and Wagner, W. (2015). Remote sensing time series revealing land surface dynamics: Status quo and the pathway ahead. In Remote Sensing and Digital Image Processing 22. Available at: https://doi.org/10.1007/978-3-319-15967-6_1

Lindén L., Riikonen A., Setälä H., and Yli-Pelkonen V. (2020) Quantifying carbon stocks in urban parks under cold climate conditions. Urban Forestry and Urban Greening 49. Available at: https://doi.org/10.1016/j.ufug.2020.126633

Maimaitiyiming M., Ghulam A., Tiyip T., Pla F., Latorre-Carmona P., Halik Ü., Sawut M., and Caetano M. (2014) Effects of green space spatial pattern on land surface temperature: Implications for sustainable urban planning and climate change adaptation. ISPRS Journal of Photogrammetry and Remote Sensing 89. Available at: https://doi.org/10.1016/j.isprsjprs.2013.12.010

Meng X., Cheng J., Guo H., Guo Y., and Yao B. (2022) Accuracy evaluation of the Landsat 9 land surface temperature product. IEEE Journal of Selected Topics in Applied Earth Observations and Remote Sensing 15: 8694-8703. Available at: https://doi.org/10.1109/JSTARS.2022.3212736

Mountrakis G., Im J., and Ogole C. (2011) Support vector machines in remote sensing: A review. ISPRS Journal of Photogrammetry and Remote Sensing 66(3). Available at: https://doi.org/10.1016/j.isprsjprs.2010.11.001

Nugraha I., Manan M., Astuti P., and Apriadi A. (2022) The Application of Participatory Mapping to Support Boundary Conflict Solving in Indonesia (Study Case: Rambah Sub Districts, Riau Province, Indonesia). Journal of Urban Regional Planning and Sustainable Environment 1(1).

Nurwanda A., and Honjo T. (2020) The prediction of city expansion and land surface temperature in Bogor City, Indone-

sia. Sustainable Cities and Society 52. Available at: https://doi.org/10.1016/j.scs.2019.101772

Babalola O. S., and Akinsanola A. A. (2016) Change Detection in Land Surface Temperature and Land Use Land Cover over Lagos Metropolis, Nigeria. Journal of Remote Sensing and GIS 5(3). Available at: https://doi.org/10.4172/2469-4134.1000171

Osuna E., Freund R., and Girosi F. (1997) Training support vector machines: An application to face detection. Proceedings of the IEEE Computer Society Conference on Computer Vision and Pattern Recognition. Available at: https://doi.org/10.1109/CVPR.1997.609310

Rahman G., Chandio N. H., Moazzam M. F. U., and Al Ansari N. (2023) Urban expansion impacts on agricultural land and thermal environment in Larkana, Pakistan. Frontiers in Environmental Science 11. Available at: https://doi.org/10.3389/fenvs.2023.1115553

Ranagalage M., Estoque R. C., and Murayama Y. (2017) An urban heat island study of the Colombo Metropolitan Area, Sri Lanka, based on Landsat data (1997-2017). ISPRS International Journal of Geo-Information 6(7). Available at: https://doi.org/10.3390/ijgi6070189

Roy S., Pandit S., Eva E. A., Bagmar M. S. H., Papia M., Banik L., Dube T., Rahman F., and Razi M. A. (2020) Examining the nexus between land surface temperature and urban growth in Chattogram Metropolitan Area of Bangladesh using long term Landsat series data. Urban Climate,32. Available at: https://doi.org/10.1016/j.uclim.2020.100593

Siddique M. A., Dongyun L., Li P., Rasool U., Khan T. U., Farooqi T. J. A., Wang L., Fan B., and Rasool M. A. (2020) Assessment and simulation of land use and land cover change impacts on the land surface temperature of Chaoyang District in Beijing, China. PeerJ 2020(3). Available at: https://doi.org/10.7717/peerj.9115

Sobrino J. A., and Raissouni N. (2000) Toward remote sensing methods for land cover dynamic monitoring: Application to Morocco. International Journal of Remote Sensing 21(2). Available at: https://doi.org/10.1080/014311600210876

Sunarta I. N., and Saifulloh M. (2022a) Coastal Tourism: Impact For Built-Up Area Growth And Correlation To Vegetation And Water Indices Derived From Sentinel-2 Remote Sensing Imagery. GeoJournal of Tourism and Geosites 41(2): 509-516. https://doi.org/10.30892/gtg.41223-857

Sunarta I. N., and Saifulloh M. (2022b) Spatial Variation Of NO2 Levels During The Covid-19 Pandemic in the Bali Tourism Area. Geographia Technica 17(1). Available at: https://doi.org/10.21163/GT_2022.171.11

Sunarta I. N., Suyarto R., Saifulloh M., Wiyanti W., Susila K. D., and Kusumadewi L. G. L. (2022) Surface Urban Heat Island (Suhi) Phenomenon in Bali and Lombok Tourism Areas Based on Remote Sensing. Journal of Southwest Jiaotong University 57(4). https://doi.org/10.35741/issn.0258-2724.57.4.44

Talukdar S., Singha P., Mahato S., Pal S., Liou Y. A., and Rahman A. (2020) Land-use land-cover classification by machine learning classifiers for satellite observations-A review. Remote Sensing 12(7): 1135. Available at: https://doi.org/10.3390/rs12071135

Trigunasih N. M., and Saifulloh M. (2022) The Investigating Water Infiltration Conditions Caused by Annual Urban Flooding Using Integrated Remote Sensing and Geographic Information Systems. Journal of Environmental Management and Tourism 13(5): 1467-1480. https://doi.org/10.14505/jemt.v13.5(61).22

USGS Earth Explorer (2023). Available at: https://earthexplorer.usgs.gov/ (accessed 24 December 2023).

Wang J., Bretz M., Dewan M. A. A., and Delavar M. A. (2022) Machine learning in modelling land-use and land cover-change (LULCC): Current status, challenges and prospects. Science of the Total Environment 822: 153559. Available at: https://doi.org/10.1016/j.scitotenv.2022.153559

Weng Q. (2009) Thermal infrared remote sensing for urban climate and environmental studies: Methods, applications, and trends. ISPRS Journal of Photogrammetry and Remote Sensing 64(4). Available at: https://doi.org/10.1016/j.isprsjprs.2009.03.007

Weng Q., Lu D., and Schubring J. (2004) Estimation of land surface temperature-vegetation abundance relationship for urban heat island studies. Remote Sensing of Environment 89(4). Available at: https://doi.org/10.1016/j.rse.2003.11.005

Wirayuda I. K. A. K., Widayani P., and Sekaranom A. B. (2023) Urban Green Space Analysis and its Effect on the Surface Urban Heat Island Phenomenon in Denpasar City, Bali. Forest and Society 7(1): 150-168. Available at: https://doi.org/10.24259/fs.v7i1.24526

Xiao J., Chevallier F., Gomez C., Guanter L., Hicke J. A., Huete A. R., Ichii K., Ni W., Pang Y., Rahman A. F., Sun G., Yuan W., Zhang L., and Zhang X. (2019) Remote sensing of the terrestrial carbon cycle: A review of advances over 50 years. Remote Sensing of Environment 233. Available at: https://doi.org/10.1016/j.rse.2019.111383

Yang J., Gong P., Fu R., Zhang M., Chen J., Liang S., Xu B., Shi J., and Dickinson R. (2013) The role of satellite remote sensing in climate change studies. Nature Climate Change 3(10). Available at: https://doi.org/10.1038/nclimate1908

Zhou L., Hu F., Wang B., Wei C., Sun D., and Wang S. (2022) Relationship between urban landscape structure and land surface temperature: Spatial hierarchy and interaction effects. Sustainable Cities and Society 80. Available at: https://doi.org/10.1016/j.scs.2022.103795

This article is an Open Access article distributed under the terms and conditions of the Creative Commons Attribution 4.0 (CC BY 4.0) License (http://creativecommons.org/licenses/by/4.0/).